



**HAL**  
open science

## **Influence of steady and oscillating swirl on the near-field spray characteristics in a two-fluid coaxial atomizer**

Nathanaël Machicoane, Guillaume Ricard, Rodrigo Osuna-Orozco, Peter Dearborn Huck, Alberto Aliseda

► **To cite this version:**

Nathanaël Machicoane, Guillaume Ricard, Rodrigo Osuna-Orozco, Peter Dearborn Huck, Alberto Aliseda. Influence of steady and oscillating swirl on the near-field spray characteristics in a two-fluid coaxial atomizer. *International Journal of Multiphase Flow*, 2020, pp.103318. 10.1016/j.ijmultiphaseflow.2020.103318 . hal-02616492

**HAL Id: hal-02616492**

**<https://hal.science/hal-02616492>**

Submitted on 24 May 2020

**HAL** is a multi-disciplinary open access archive for the deposit and dissemination of scientific research documents, whether they are published or not. The documents may come from teaching and research institutions in France or abroad, or from public or private research centers.

L'archive ouverte pluridisciplinaire **HAL**, est destinée au dépôt et à la diffusion de documents scientifiques de niveau recherche, publiés ou non, émanant des établissements d'enseignement et de recherche français ou étrangers, des laboratoires publics ou privés.

# Influence of steady and oscillating swirl on the near-field spray characteristics in a two-fluid coaxial atomizer

Nathanael Machicoane<sup>a</sup>, Guillaume Ricard<sup>a</sup>, Rodrigo Osuna-Orozco<sup>a</sup>, Peter Dearborn Huck<sup>a</sup>, Alberto Aliseda<sup>a</sup>

<sup>a</sup>*University of Washington, Department of Mechanical Engineering, Seattle, WA 98105, USA*

---

## Abstract

The mechanisms of interfacial instability due to gas-liquid shear and liquid ligament acceleration that occurs in the near-field of a coaxial two-fluid atomizer play a determining role on the spray characteristics in the far-field, making understanding of these near-field physics key for spray modeling. Several metrics for these physical processes, with an emphasis on the liquid core length, are characterized in detail, using high-speed shadowgraphy, over a wide range of gas-to-liquid momentum ratios, comparing the fluids' dynamic pressures at the exit of the atomizer. A method that does not require arbitrary thresholds is proposed to rigorously define the initial spreading angle of a spray. The effect of adding azimuthal momentum to the gas co-flow (swirl) on the spray near-field is analyzed, and the possibility of periodic oscillations of the swirl is explored. Increased spreading angle is expected when swirl is present, but a decrease of the liquid core length average and standard deviation is also observed, with variations happening over timescales shorter than the actuation period. The overall effect is a wider, more dynamic spray,

---

*Email address:* nmachico@uw.edu (Nathanael Machicoane)

that present a dramatic decrease in characteristic droplet sizes. At high momentum and swirl ratios, while the effects on the liquid core length follow similar trends, the temporal evolution is largely modified by the development of long-time dynamics, attributed to a vortex formed by recirculating gas downstream of the liquid core on the spray centerline, that becomes unstable and penetrates inside the liquid nozzle. Oscillations of the swirl have little effect on the mean spray structure, as the oscillation frequency is decorrelated from the spray timescales. While the liquid core length may seem to present quasi-steady dynamics, the maxima never exceed the lengths obtained for a steady case, when the swirl equals the value at the trough of the oscillations, while the minima are below what would be observed for the spray under steady conditions equal to the peak of value of the swirl and momentum ratios. Variations of the intact length around the quasi-equilibrium state present similar magnitude and timescale as the steady cases.

*Keywords:* atomization, coaxial two-fluid atomizer, spray, swirl, high-speed shadowgraphy, liquid core length

---

## 1. Introduction

Two-fluid atomization is an important part of many engineering processes, for instance in manufacturing or propulsion. In these applications, many other physical mechanisms come into play, such as thermal and/or chemical phenomena. A complete characterization of such a multi-scale turbulent multi-phase flow, allowing for the level of modeling required in these applications, is still lacking. Several decades of research have led to a good understanding of the different atomization regimes that take place over the in-

herently wide range of parameters [Chigier and Reitz, 1996; Lasheras and Hopfinger, 2000]. The region near the exit of the atomizer, referred to as the near-field, where the liquid is being destabilized and broken into drops, ligaments and sheets, has been shown to play a large role on the spray formation and its modeling [Gorokhovski and Herrmann, 2008]. The difference of velocity between the two fluids leads to longitudinal and transverse instabilities at the interface [Marmottant and Villermaux, 2004]. These instabilities then play a crucial role in determining the droplet size distributions of the spray [Aliseda et al., 2008; Lasheras et al., 1998; Varga et al., 2003]. A more thorough characterization of the near-field is necessary to reach the statistical description needed for modeling and also to provide data to help with the validation of the recent numerical approaches [Krolick and Owkes, 2018; Ling et al., 2019; Odier et al., 2018; Vu et al., 2018]. Metrics have often been reported for specific atomizers, and both their definitions and their proposed correlations with spray parameters can diverge widely. For instance, the flapping or helicoidal instability was reported almost three decades ago [Eroglu et al., 1991], and despite having been described extensively [Engelbert et al., 1985; Juniper and Candel, 2003; Leroux, 2007], its physical origin, as well as its scaling with relevant parameters, has only been proposed recently [Delon et al., 2018].

Among the characteristics of the near-field of sprays, the liquid core length has been pointed out as one of the most important parameters to characterize the break-up and attempt its modeling [Bracco, 1985; Chigier, 1981; Lefebvre, 1989]. It represents a crucial metric for many applications such as combustion. For two-fluid coaxial atomizers, where the atomization of a liquid jet into a spray is assisted by a gas co-flow, the liquid core length is defined

as the longitudinal extent of the intact liquid portion that is still connected to the nozzle, sometimes also referred to as intact core, in opposition to the remaining liquid inclusions (drops, ligaments, sheets and droplets) that are fully detached from the atomizer. The break-up of the liquid core in two-fluid atomization results in a non-linear interaction between the two phases, and since at least one of them is highly turbulent and presents high intermittency large fluctuations are expected. In early work, several pictures were collected for each condition and then only average quantities were reported in order to reduce measurement noise [Arai and Hashimoto, 1985]. [Eroglu et al., 1991] commented, however, on finding large deviations for the liquid core length, reporting fluctuations around the mean of the order of 15%. Despite this comment, and comments about the time-dependent, pulsating, nature of sprays [Chigier and Farago, 1992], average values have been predominantly reported in recent investigations. Even when using an advanced measurement method, [Charalampous et al., 2009] showed fluctuations of the order of 10% around the mean. Recently, [Kumar and Sahu, 2018] used series of instantaneous measurements of the liquid core length to derived the mean and standard deviation values, but also to report distributions that better characterize its variations. The parameter capturing the evolution of the liquid core length versus spray parameters is, for given fluids (i. e. for a given surface tension), the gas-to-liquid momentum ratio,  $M$ , that compares the dynamic pressure of the gas to that of the liquid. The range of momentum ratios explored by [Kumar and Sahu, 2018] is very narrow ( $M = 1$  to 8), and the temporal dynamics of the core length is not studied. The latter has been lacking in the literature, missing a converged statistical descrip-

tion, up to recent efforts [Charalampous et al., 2019], in a low and narrow range of gas-to-liquid momentum ratios ( $M = 1$  to 8, extracted from the reference’s data). This paper contributes to the understanding of this class of sprays by providing a novel statistical description over a wide range of momentum ratios, along with a robust description of the spray near-field structure based on a rigorous method to define the spray spreading angle. While the former mostly targets modeling purposes, the methods as well as the data generated in the canonical configuration investigated here can serve to validate the upcoming numerical simulations that are now made possible thanks to the recent advances in numerical methods of turbulent multiphase flow [Kannan et al., 2018; Ling et al., 2019; Owkes et al., 2018; Wand and Desjardins, 2018]. Exploring coaxial atomization on a wide range of momentum ratio means that several break-up modes will be encountered; , which are well described in [Dumouchel, 2008; Lasheras and Hopfinger, 2000; Marmottant and Villermaux, 2004]. For coaxial atomization with laminar liquid injection as considered here, bag and fiber-type break-up modes are present, respectively for low and high momentum ratio, with a transition around  $M = 26$  as described in[Lasheras and Hopfinger, 2000].

A second contribution from this paper is to further characterize the effect of angular momentum in the gas co-flow, referred to as swirl, on the spray near-field. Swirl is present in many applications [Lilley, 1977] and has recently been shown to have dramatic effect on the time dynamics of the flow of hollow cone sprays [Rajamanickam and Basu, 2017]. However, its study is incomplete for coaxial two-fluid atomization, despite an extensive literature for swirling jets [Billant et al., 1998; Gallaire and Chomaz, 2003;

Liang and Maxworthy, 2005] and gas-gas coaxial flows [Santhosh et al., 2013]. Since the first report of the striking effect of swirl addition in the gas co-flow [Hopfinger and Lasheras, 1996], notably on the spray spreading angle, the few follow-up investigations have been summarized in a two-decade-old review [Lasheras and Hopfinger, 2000]. In particular, the droplet size in the far-field is seen to decrease in the center of the spray, while it is slightly increased at its edge. For both angle and droplet size, a threshold (that converges down towards to an asymptotic value as  $M$  grows) in swirl addition is needed to see dramatic effects. The existence of the threshold is explained in term of a balance between the low pressure caused by azimuthal motion and the dynamic pressure of the multiphase flow on the spray center-line, that can create a recirculating region downstream of the liquid core. At low swirl, no recirculation is present behind the liquid core, while it causes lateral expansion at high swirl, which was referred to as explosive break-up [Hopfinger and Lasheras, 1996]. [Machicoane et al., 2019] proposed, based on Synchrotron high-speed radiography, that, at high enough swirl and momentum ratios, this vortex can also *i)* trigger a transition of the liquid core to a more dynamic state where the core is hollow in its center and sheds ligaments from its periphery, and *ii)* can become unstable and rests off-center from the atomizer axis, presenting long-time dynamics where it orbits around this axis. The effect of swirl addition in the gas co-flow needs to be studied in more detail, in the canonical context of two-fluid coaxial atomization, to understand more clearly these complex dynamics and their physical origin, as well as their impact on the spray characteristics, both in the near and far-field. In addition to this, we briefly discuss how slow temporal oscillations of

the swirl can further affect the spray features, in an effort to shed light on the underlying mechanisms that can occur when real-time feedback control of atomization is performed [Osuna-Orozco et al., 2019].

The paper is organized as follows: the canonical atomizer and its operating conditions, as well as the imaging setup are presented in section 2. The spray characteristics in the near-field are introduced in section 3, and their evolution with momentum and swirl ratios are presented in section 4. The results and their implications are discussed in section 5, followed by conclusions (section 6).

## 2. Experimental setup

### 2.1. A canonical atomizer

The spray is produced by an open-source canonical two-fluid coaxial atomizer<sup>1</sup>, sketched in Figure 1 and described in detail in [Machicoane et al., 2019]. Liquid is injected in the center of the atomizer, through a long duct where it reaches fully-developed Poiseuille flow, at a fixed flow rate  $Q_l$  yielding laminar flow. The liquid Reynolds number, based on inner liquid nozzle diameter  $d_l = 2$  mm and the mean exit liquid velocity  $U_l = Q_l/A_l$  with  $A_l = \pi d_l^2/4$ , is  $Re_l = U_l d_l/\nu_l \simeq 1200$ , where  $\nu_l$  is the kinematic viscosity of water at 25°C. The liquid nozzle is positioned at the centerline of a gas nozzle, both presenting cubic-spline shaped walls. Eight inlets guide gas into the nozzle, as depicted in Figure 1b). Their positions with respect to the axis of the

---

<sup>1</sup>The complete 3D geometry can be found at <http://depts.washington.edu/fluidlab/nozzle.shtml>.

atomizer can produce a gas jet that either has no or some angular momentum (referred to as swirl). The former is achieved when flow is only injected through the on-axis inlets at a rate  $Q_{NS}$  and the latter when the flow rate  $Q_{SW}$  through the off-axis inlets is non-zero. To study the effect of swirl addition on the spray, while keeping other parameters relevant to the atomization processes fixed, the total gas flow rate  $Q_{Total} = Q_{NS} + Q_{SW}$  is kept constant, and the amount of swirl is described by the swirl ratio  $SR = Q_{SW}/Q_{NS}$ , with  $0 < SR < 1$  here. The gas Reynolds number  $Re_g = 4Q_{Total}/\sqrt{4\pi A_g}\nu_g$  ranges from approximately  $2 \cdot 10^4$  to  $9 \cdot 10^4$ , where  $\nu_g$  is the kinematic viscosity of air at  $25^\circ\text{C}$  and  $A_g = \pi(d_g^2 - D_l^2)/4$ , with  $D_l = 3$  mm and  $d_g = 10$  mm are the liquid nozzle outer and gas nozzle inner diameters.

Besides the effect of a steady swirl component, the study investigates angular momentum modulated in time. The use of proportional valves, that control and fix the gas flow rate, permits quasi-sinusoidal oscillations at a period of 2.2 s. This forcing period is much slower than any relevant timescale of the spray dynamics, but is applied to test possible deviations from a quasi-steady behavior of the spray to modification of the input parameters, in the context of real-time feedback control investigations [Osuna-Orozco et al., 2019]. We consider a constant no-swirl flow rate  $Q_{NS}$ , while the swirl flow rate varies from  $Q_{SW} = 0$  to  $Q_{SW} = Q_{NS}$ , maintaining a total flow rate  $\langle Q_{Total} \rangle$  and swirl ratio  $\langle SR \rangle = 0.5$  constant when averaged over a period, while their instantaneous values do vary in time.

Along with the swirl ratio  $SR$ , the gas-to-liquid momentum ratio  $M$  is used to characterize changes in the total gas flow rate. It compares the dynamic pressure of the gas to the liquid's and is defined as  $M = \rho_g U_g^2 / \rho_l U_l^2$

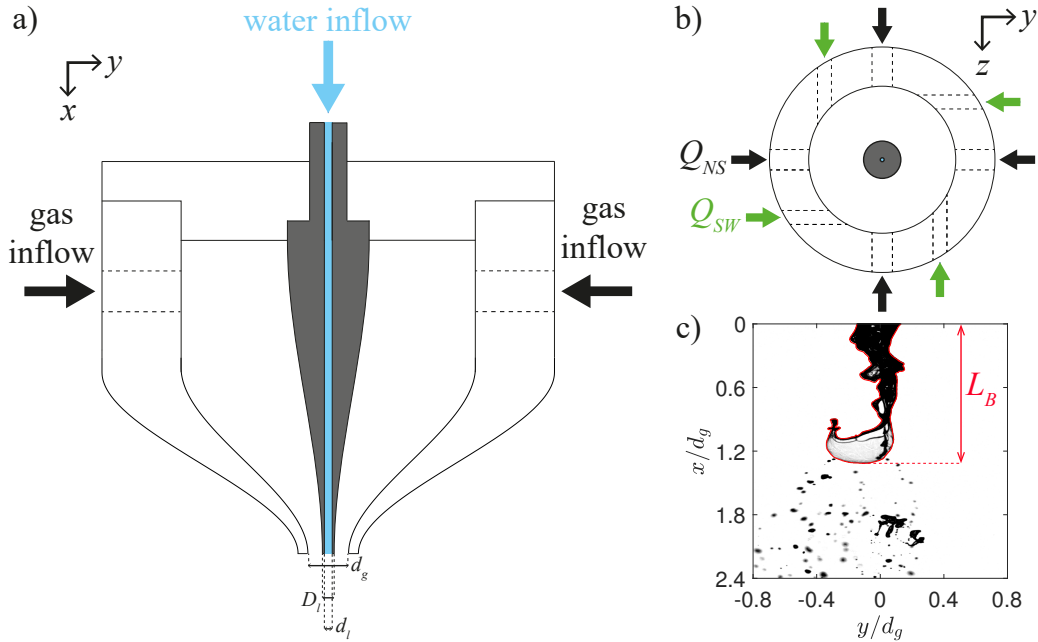


Figure 1: (color online) Longitudinal (a) and transverse (b) cuts of the coaxial two-fluid atomizer (the complete 3D geometry is open-source and available at <http://depts.washington.edu/fluidlab/nozzle.shtml>). Water is injected in the center of the atomizer, while gas enters the nozzle through 8 inlets in a horizontal plane. It then flows along the cubic-spline-shaped walls inside the atomizer. Four inlets are on the atomizer's axis and produce a longitudinal gas co-flow while four others are off-axis and induce angular momentum in the gas jet produced at the exit of the atomizer. The atomizer axis is vertical, pointing downward, and is denoted  $x$ . c) Back-lit image of the spray for  $M = 5.3$  and  $SR = 0$ , covering a field of view of  $2.4 \times 1.6 d_g^2$ , with a resolution of  $2.7 \cdot 10^{-3} d_g$  ( $27 \mu\text{m}$ ). The camera axis  $z$  is perpendicular to  $x$ , yielding images in the longitudinal plane  $(x, y)$ . The image was background-corrected and the grayscale goes from 0 to 1. The red contour correspond to the liquid core and is obtained through image processing; its longitudinal extent defines the liquid core length  $L_B$ .

$U_g$ (m/s)	$Re_g$	$M$	$m$	$We_{d_l}$
35	21 400	5.27	0.56	39.1
51.3	31 400	11.3	0.38	84.8
76.7	47 000	25.4	0.25	191
114	70 000	56.2	0.17	426
138	84 300	81.5	0.14	618

Table 1: Flow parameters for fixed laminar liquid injection ( $Re_l \simeq 1200$ ), varying the total gas flow rate. The mean gas velocity  $U_g = Q_{Total}/A_g$ , the gas Reynolds number is  $Re_g = 4Q_{Total}/\sqrt{4\pi A_g}\nu_g$ , the gas-to-liquid momentum ratio is  $M = \rho_g U_g^2/\rho_l U_l^2$ , the liquid mass loading is  $m = \rho_l A_l U_l/\rho_g A_g U_g$  and the Weber number is based on the liquid diameter as  $We_{d_l} = \rho_g(U_g - U_l)^2 d_l/\sigma$ . The fluids are air and distilled water, at an ambient temperature of 25°C, with kinematic viscosities of  $\nu_g = 1.56 \cdot 10^{-5} \text{ m}^2 \text{ s}^{-1}$  and  $\nu_l = 8.96 \cdot 10^{-7} \text{ m}^2 \text{ s}^{-1}$ , densities  $\rho_g = 1.18 \text{ kg m}^{-3}$  and  $\rho_l = 996.9 \text{ kg m}^{-3}$ , and the air-water surface tension  $\sigma = 72 \text{ mN m}^{-1}$ .

( $M > 1$  here), with  $U_g = Q_{Total}/A_g$  and  $\rho_l$  and  $\rho_g$  the liquid and gas densities. For completeness, we introduce other atomization parameters, with their values over the parameter space listed in Table 1. The liquid mass loading, comparing liquid to gas mass flow rates,  $m = \rho_l A_l U_l/\rho_g A_g U_g$  is smaller than unity. The Weber number, based on the average exit velocities and the liquid inner diameter,  $We_{d_l} = \rho_g(U_g - U_l)^2 d_l/\sigma$  ranges between 40 and 700, where  $\sigma$  is the liquid-gas surface tension. For coaxial atomization in the absence of swirl, the first two lines of Table 1 are expected to present bag break-up modes, the last two rows present fiber-type atomization, while the intermediate case of  $M = 25.4$  has mixed modes.

## 2.2. High-speed shadowgraphy

A bright light source, with its axis perpendicular to the spray axis, illuminates the spray immediately downstream of the nozzle. A high-speed camera is placed along the light's axis, on the other side of the spray, to capture sequences of shadowgraphy images. The temporal and spatial resolutions for this study are 0.1 ms and 27  $\mu\text{m}$  respectively. The recording duration for each condition is about 1 second, several hundred times longer than the slower processes of the spray, and the field of view is approximately 2.4 times the gas diameter  $d_g$  in the longitudinal direction, and 1.6 times in the transverse direction, with a depth of field of about  $0.6d_g$ . When swirl oscillations are considered, the temporal resolution is decreased by a factor of 10 to allow for a longer duration, due to limitations of the camera's on-board memory. This yields a duration of about 4 periods.

A background correction, consisting of a subtraction followed by a division, yields quasi-binary images where the liquid core has values of 1, while the background is at 0. A simple thresholding with any value in between permits the identification of the spray edge (0.5 was chosen arbitrarily, but no significant sensitivity to the threshold was observed in the range 0.05 to 0.95). Figure 1c) shows a typical image, where this threshold was used to define the boundary of the liquid core (red contour). Any pixel value above the threshold is considered as a good estimate of liquid presence in the measurement volume. One can note that, in opposition to more advanced techniques such as X-ray absorption where the measured intensity can relate to the amount of liquid present [Kastengren and Powell, 2014; Heindel, 2019; Li et al., 2019], the binary image obtained here only indicates liquid's presence or absence,

but not the amount of liquid in the line of sight. The detection accuracy of the liquid core length on each image, from the image processing tools used, is about 30 times less than the minimal intact length detected (accurate to  $0.08d_g$ ). The mean liquid core length converges statistically to within 0.1%.

An ensemble average of many thresholded images is then used to measure the probability  $P$  of finding liquid, whether part of the intact core or broken up into drops, sheets or ligaments, at a given location along the spray development region. A probability  $P = 0$  means that liquid is never observed there, while 1 corresponds to liquid being always present (a region that has been defined as the spray core cone, due to its shape for a coaxial atomizer, [Lasheras and Hopfinger, 2000]). Intermediate values indicate an alternation between presence and absence of liquid, which can be observed along the spray core, due to flapping motion and break-up events, and downstream of the liquid core, where drops, sheets or ligaments undergo turbulent dispersion and secondary break-up. Similarly, the standard deviation of the ensemble of images yields the variations of liquid presence,  $P'$ , that accounts for the unsteady nature of this turbulent multiphase flow.  $P' = 0$  within the spray core cone, as liquid is always present, and also outside of the spray boundaries where liquid is never present. The variation would be maximum and equal to  $P' = 0.5$  at locations where there is liquid present at a given location every other image, as liquid inclusions are shed from the liquid core. When liquid is either present, or not present a fifth of the time,  $P' = 0.4$ , which can be used as an empirical threshold to visualize very active regions of the spray that include events such as shedding, flapping and convection and growth of interfacial instabilities.

Despite the shortcoming of visible light imaging to define the liquid core boundary described in [Charalampous et al., 2007], shadowgraphy remains accurate in the range of momentum ratios explored here, due to the low liquid mass loading considered. Comparisons with Synchrotron high-speed X-ray absorption imaging [Machicoane et al., 2019] indeed yield very good agreement (the inset of Fig. 8b) shows a typical back-lit image for the most dynamic condition explored in this range), and slight differences only start to appear for  $M > \mathcal{O}(100)$ . In this regime, the liquid core is hollow almost up to the atomizer exit plane and sheds ligaments from its periphery in a very active manner, which can obscure light even at low mass loading values. This part of the parameter space was deemed to be out of the range of typical applications and would required more advanced methods, not based on visible light, to be properly studied.

### 3. Spray characteristics

#### 3.1. Instantaneous liquid core length

From the detection of the liquid core obtained with the described image processing, we define the instantaneous liquid core length  $L_B$ , on each image, as the longitudinal extent of the liquid core (see Fig. 1c)). The frame-rate is high enough to resolve the temporal dynamics of  $L_B$  and enough snapshots are captured to study its statistics. Figure 2a) shows the probability density function (PDF) of the liquid core length normalized by the gas nozzle inner diameter  $d_g$ , for three conditions:  $M = 25$  with  $SR = 0$  and 0.5 as well as ( $M = 80, SR = 0$ ). The supplementary materials contain a snapshot movie corresponding to each condition, emphasizing the effect of increase

of momentum and swirl ratios on the spray spatial and temporal dynamics. Figure 3 shows sample images for these conditions. The PDFs are divided by their maximum value for visibility. The distributions are non-Gaussian, with stronger probability to have larger values and less probability to have smaller values than a Gaussian process; the PDFs are positively skewed. They are roughly well-fitted by log-normal distributions, although with fitting parameters differing from the average and standard deviation of the logarithm of the signal. In the absence of swirl, increasing the gas-to-liquid momentum ratio  $M$  from 25 to 80, decreases the location of the maximum by 40% (lower liquid core lengths) and drastically reduces the spread of the distribution. It also slightly decreases the skewness, that is, the distribution at high  $M$  is closer to Gaussian. For a fixed momentum ratio, the addition of swirl, going from  $SR = 0$  to  $SR = 0.5$ , has a similar effect as a slight increase of momentum ratio  $M$ , decreasing the location of the maximum by 20%, and slightly decreasing the spread of the distribution and bringing it closer to Gaussian.

While the PDF fully describes the statistics of the liquid core length values, it does not contain any information on its time variations. We first turn to the power spectral density (PSD) of the time series of  $L_B$ , displayed in Fig. 2b) for the same conditions. The PSDs present a plateau in the low-frequency range, which means that the signal is fully decorrelated at long times. At high frequencies, the PSDs have approximately the same power law decay (with an exponent equals to roughly  $-7/8$ ). For low momentum ratio, regardless of the presence of swirl, a clear, although wide, peak is present, allowing for the identification of a characteristic frequency. This frequency relates to

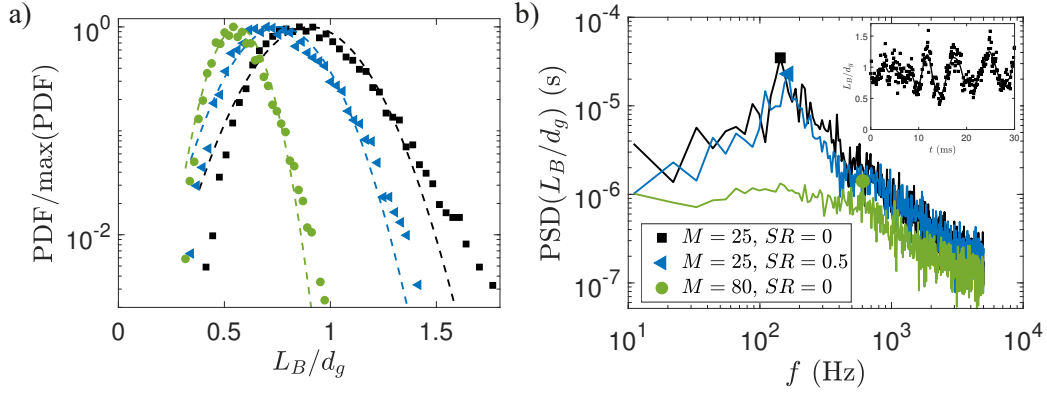


Figure 2: (color online) a) Probability density function (PDF) of the liquid core length  $L_B$  normalized by the gas nozzle diameter  $d_g$ ; the PDFs are normalized by their maximum value for clarity. The dashed lines correspond to Gaussian distributions defined by the mean and standard deviation of the liquid core length for each condition. b) Power spectral density (PSD) of  $L_B/d_g$ . The time series of  $L_B$  is cut in 10 pieces, each yield a PSD that are then averaged together to increase the signal-to-noise ratio in the frequency range of interest. The inset shows a small portion of the typical time-series of the liquid core length for ( $M = 25, SR = 0$ ). The symbols ( $\blacksquare$ ,  $\blacktriangleleft$ ,  $\bullet$ ) show the locations of the maxima of the PSDs, respectively at 142.9; 164.8 and 604.4 Hz (with a resolution of 11 Hz) for ( $M = 25, SR = 0$ ); ( $M = 25, SR = 0.5$ ) and ( $M = 80, SR = 0$ ).

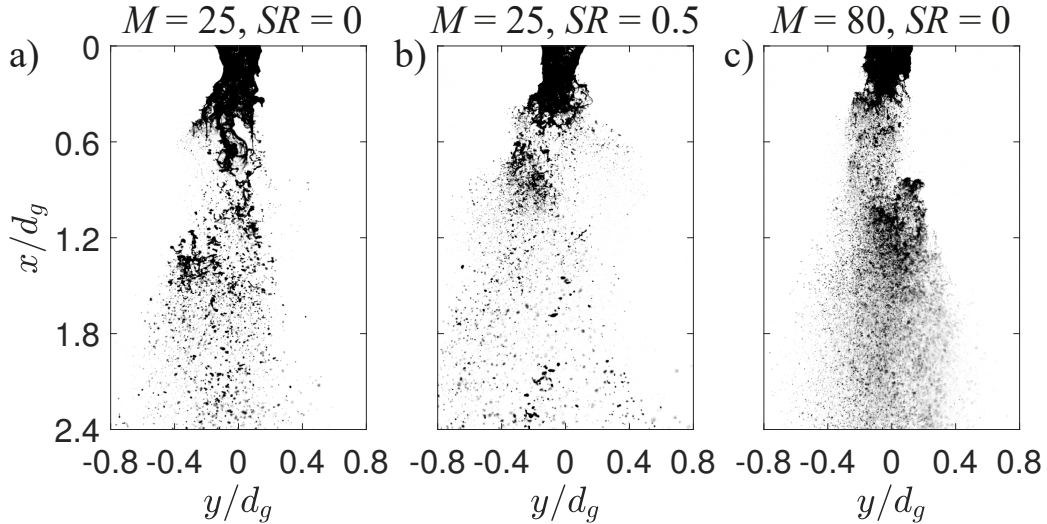


Figure 3: Back-lit images of the spray for a) ( $M = 25$ ,  $SR = 0$ ), b) ( $M = 25$ ,  $SR = 0.5$ ) and c) ( $M = 80$ ,  $SR = 0$ ). The images were background-corrected and the grayscale goes from 0 to 1.

bursts of liquid inclusions being periodically shed from the intact core. The time-series in the inset of Fig. 2b) shows this typical evolution, where the intact length increases and then decreases, in a quasi-periodic fashion that was referred to as a pulsating dynamic [Chigier and Farago, 1992]. Swirl addition increases this frequency by 15%; the liquid core is then shorter on average, with less variations, happening over shorter periods. For  $M = 80$ , if a characteristic frequency is present, it occurs towards higher frequencies, where it lies in the power law decay range. While a maximum of the PSD can still be detected, for a frequency about 400% higher than for  $M = 25$ , it is questionable whether this really represents the time dynamics of the liquid core length for these conditions. Several other peaks seem to emerge in this range of frequencies, with values only slightly lower, making the choice of this

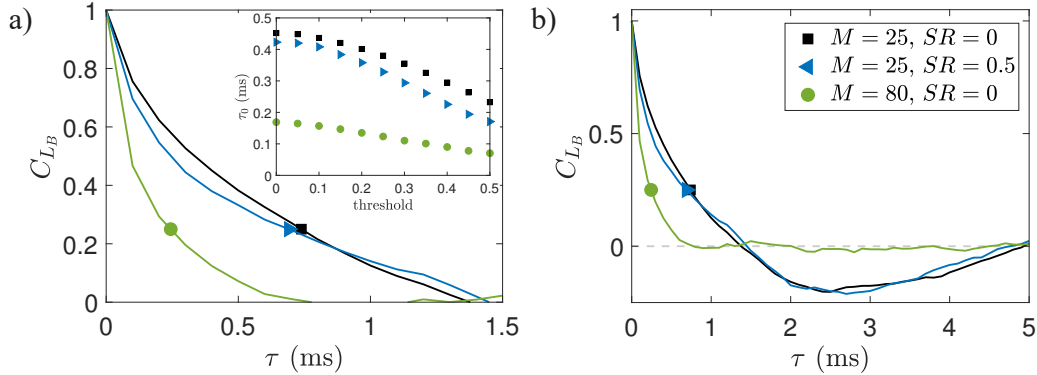


Figure 4: (color online) Auto-correlation of the liquid core length  $L_B$  over a narrow (a) and wider (b) range of time-lags  $\tau$ . The symbols (■, ◀, ●) show the times at which the functions reach a threshold of 0.25, respectively at 0.74, 0.69 and 0.24 ms for ( $M = 25$ ,  $SR = 0$ ); ( $M = 25$ ,  $SR = 0.5$ ) and ( $M = 80$ ,  $SR = 0$ ). The inset of (a) represents the liquid core length timescale  $\tau_0$ , computed as the integral of the auto-correlation function up to the time at which it reaches a threshold value (varied between 0 to 0.5).

peak over the other slightly arbitrary (although it is not user-dependent).

Instead of considering the power spectra, we can extract the liquid core length time-scales through the use of the auto-correlation function of  $L_B(t)$  (the PSD is the Fourier transform of this function). It is defined, in its normalized form, as  $C_{L_B}(\tau) = \langle L_B(t)L_B(t + \tau) \rangle / L_B'^2$ , where  $\tau$  is the time-lag and  $L_B' = \sqrt{\langle L_B^2 \rangle - \langle L_B \rangle^2}$  is the standard deviation of  $L_B$ . It gives a direct measurement of the time necessary for variations of the intact length to become uncorrelated, representing a characteristic time-scale over which they happen. A simple statistical description of the liquid core length can then be its mean value  $\langle L_B \rangle$ , which is also roughly its most probable value given the slightly skewed PDF's shape, combine with the magnitude of its fluctuations,  $L_B'$ , along with the fluctuations time-scale,  $\tau_0$ , which needs to

be extracted from  $C_{L_B}$ . Figure 4 shows the auto-correlation function for  $L_B$  (a) zoomed-in, b) over a large range of time-lags, for the three conditions from Fig. 2. One can first note, that at a high momentum ratio, the function decreases asymptotically toward zero, while lower momentum ratio functions pass zero to a minimum and then slowly increase toward zero. This is due to the strong periodic behavior of the signal that is only present for low  $M$  (as shown with the PSD). As expected, the decorrelation is much faster for  $M = 80$  than for  $M = 25$  in the absence of swirl, and swirl addition slightly increases the rate at which decorrelation occurs, with the function decreasing faster towards zero initially. However, the shape of the function is different in the presence of swirl, with the decorrelation slowing down for shorter time-lags than in the absence of swirl, making the functions cross. To take into account the change of shape of the functions with spray parameters, we define the correlation time  $\tau_0 = \int_0^{\tau_T} C_{L_B}(\tau)d\tau$ , where  $\tau_T$  is such that  $C_{L_B}(\tau_T) = \text{threshold}$ , a threshold that needs to be defined. The inset of Fig. 4a) shows the evolution of  $\tau_0$  with the value of the threshold, between 0 and 0.5 (full to 50% decorrelation). The time-scales consistently follow the same order:  $(M = 25, SR = 0)$ ;  $(M = 25, SR = 0.5)$  and  $(M = 80, SR = 0)$ , irrespective of the choice of threshold's value, and the ratios between the times vary only slightly in the range 0.2 to 0.5. A threshold of 25% was chosen to keep the ratio of 1.15 between the time-scales for  $(M = 25, SR = 0)$  and  $(M = 25, SR = 0.5)$ , where the peaks in the PSD are clearly identified (yielding periods of the liquid core length of 7 and 6.07 respectively). This does not preserve the ratio between  $M = 25$  and  $M = 80$  (period of 1.65 ms from the PSD), which changes from 4.23 to 3.08. However, as discussed, the

time-scales extracted from the PSD for high momentum ratios are subject to greater uncertainty. For  $M = 25$ , both in the presence and absence of swirl, the correlation time-scale  $\tau_0$ , with a threshold of 25%, is about 20 times lower than the period extracted from the PSD. The correlation time-scale then quantifies the rate of variation of the intact length, while the frequency extracted from the PSD relates to the period at which the liquid core pulsates.

### 3.2. Spray angles

Figure 5a) shows a map of the liquid probability  $P$  for ( $M = 5$ ,  $SR = 0$ ), while Figure 5b) displays transverse profiles of  $P$ , i.e. a cut of the map along  $y$ , for several longitudinal distances  $x$  between  $\langle L_B \rangle$  and  $1.5 \langle L_B \rangle$ . At the very exit of the nozzle, the transverse profiles are roughly top-hat functions, as the probability of finding liquid is  $P = 1$  over the range  $-0.5 < x/d_l < 0.5$ . A short distance downstream,  $P(y/d_g)$  becomes self-similar, and is well represented by a Gaussian ( $R^2$ -values above 0.99 for  $x \geq 0.25d_g$  for this particular condition). This means that studying how the width of the Gaussian, or its standard-deviation  $\sigma$ , evolves with  $x$  is enough to capture the spray-spreading dynamics, in analogy with the velocity of a single-phase turbulent round jet. In other words, the change of the width of the spray can be evaluated by the evolution of  $\sigma$ , without the need to define a contour of the value of  $P$ , where the threshold value would need to be chosen, which would affect the behavior of the spreading angle. With the proposed method, while the width of the spray still needs to be defined arbitrarily, and this will affect the numerical value of the spreading angle, the reported Gaussian nature ensures that the behavior of the angle with the spray parameter remains univocally defined.

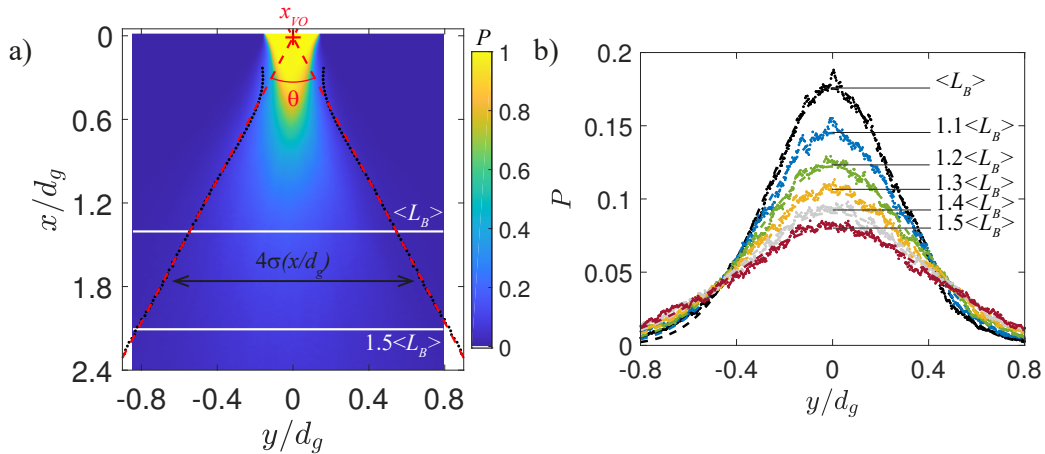


Figure 5: (color online) a) Probability of liquid presence (inferred from the back-lit images, through background subtraction, renormalization and thresholding, followed by ensemble averaging). b) Transverse profiles of the probability of liquid presence, for various longitudinal distances from the nozzle exit plane,  $\langle L_B \rangle \leq x \leq 1.5 \langle L_B \rangle$ ; they are fitted well by Gaussian distributions,  $A \exp(-(y/d_g)^2/2\sigma^2)$ , where  $A$  and  $\sigma$  are functions of  $x$ . The values of  $\pm 2\sigma(x)$  are reported on (a) by black dots when the Gaussian fits have  $R^2$  values larger than 0.99, over the range of measured longitudinal distances, shown every  $0.025 d_g$  for visibility. The function  $2\sigma(x/d_g)$  is fitted linearly, between  $\langle L_B \rangle$  and  $1.5 \langle L_B \rangle$  depicted as white lines here, to measure the spray angle  $\theta$  and virtual origin  $x_{VO}$  (where the two red dotted lines cross). The condition for a) and b) is  $M = 5$  and  $SR = 0$ .

We have chosen, for instance, to define the (full) width of the spray as  $4\sigma$ , at a given position  $x/d_g$ , establishing the spray as the region where  $P \geq 13.5\%$ , but choosing another definition will just add a constant multiplying factor to the resulting spreading angle.

For the range of conditions explored here, it was found that  $\sigma(x/d_g)$  always follows a linear behavior in the range  $\langle L_B \rangle \leq x \leq 1.5 \langle L_B \rangle$ . A linear fit then allows for the definition of the spreading angle  $\theta$  (the full cone angle for a spray of full width  $4\sigma(x/d_g)$ , as indicated in figure 5a)). The numerical

value of  $\theta$  depends on the definition of the spray width, but its behavior with the spray parameters does not. Furthermore, the linear fit also allows for the definition of a spray virtual origin,  $x_{VO}$ , which is independent of the width definition. The angle,  $\theta$ , together with the virtual origin,  $x_{VO}$ , yields a very accurate representation of the initial spreading of the spray in the near-field.

#### 4. Evolution of the spray characteristics with momentum and swirl ratios

##### 4.1. Steady swirl

Figure 6 reports the spreading angle  $\theta$  and the virtual origin  $x_{VO}$  of the spray near-field as functions of  $M$ , for different swirl ratios  $SR$ . As expected, the initial spreading angle decreases as the gas-to-liquid momentum ratio increases, in the absence of swirl. The behavior in this range is logarithmically decreasing, from  $43^\circ$  at  $M = 5$  to  $17^\circ$  for  $M = 80$ . As for the virtual origin of the velocity of a turbulent round jet,  $x_{VO} \leq 0$  which means that the origin is inside the nozzle and the spreading starts approximately at the nozzle exit. The virtual origin decays in a power law with exponent  $\approx 0.6$  as  $M$  increases. Over the range of momentum ratios, swirl addition increases the spreading angle, as reported by [Hopfinger and Lasheras, 1996], and the virtual origin, so the spreading starts slightly further downstream. However, the behavior is non-monotonic for both metrics, which is in agreement with previous work [Hopfinger and Lasheras, 1996]. At both  $M = 5$  and  $M = 25$ ,  $SR = 0.25$  yields roughly the same results as  $SR = 0$ . Over the range of  $M$ ,  $SR = 0.5$  has a dramatic effect on both the angle and the virtual origin. Further swirl addition seems to generally have no effect or the opposite effect. This could

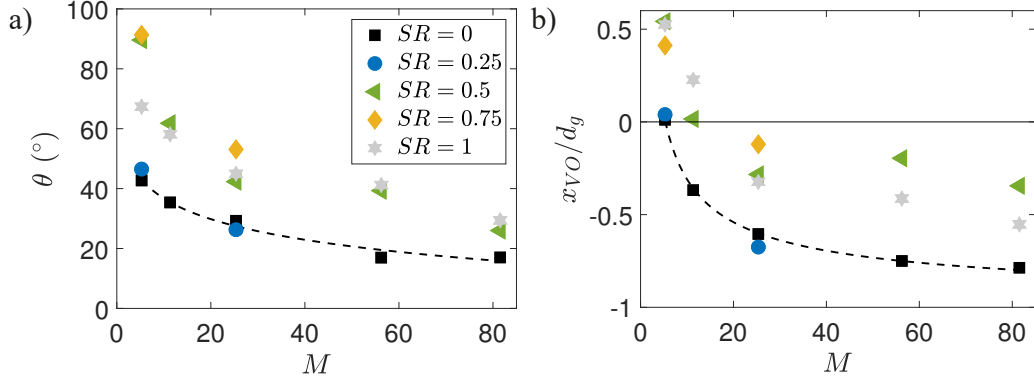


Figure 6: (color online) Evolution of the spray initial angle  $\theta$  (a) and its virtual origin  $x_{VO}$  (b) as a function of the momentum ratio  $M$ , for different swirl ratios  $SR$ . The dashed lines are fits of  $\theta(M)$  and  $x_{VO}(M)$  respectively, both in the absence of swirl ( $SR = 0$ ), with values  $\theta = 59.6 \pm 9.1 - (10 \pm 2.7) \log(M)$  and  $x_{VO}/d_g = (2.7 \pm 0.2)M^{-0.59 \pm 0.03}$ .

be attributed to vortex breakdown happening inside the nozzle, which would happen for larger swirl ratios as the gas Reynolds number (or  $M$  here as the liquid velocity is kept constant throughout the study) increases. This prevents the existence of a stable vortex downstream of the liquid core, which is responsible for the spray spreading.

Figures 7a) and b) show the evolution of the mean and standard deviation of the liquid core length,  $\langle L_B \rangle$  and  $L'_B$ , respectively, with the gas-to-liquid momentum ratio  $M$ , for various swirl ratios  $SR$ . In the absence of swirl, both quantities follow a decreasing logarithmic behavior, keeping the ratio  $L'_B/\langle L_B \rangle \simeq 20\%$ . When  $M$  increases from 5 to 80,  $\langle L_B \rangle$  is decreased by a factor of 2.5. The behavior of both quantities with swirl is, in opposition to the angle and virtual origin, monotonic, with the exception of  $SR = 1$  for  $M \leq 11$ , due to the vortex breakdown downstream of the nozzle, referenced previously. There is still no, or a small opposite, effect of  $SR = 0.25$ . The

same observations can be made of the liquid core length time-scale  $\tau_0$  (see Fig. 7c)), with the exception of the behavior at  $M = 80$ , which will be discussed below. A roughly logarithmic behavior is observed along  $M$  in the absence of swirl,  $\tau_0$  decreasing by a factor of 4.8 over the range of  $M$  explored. The general picture is, then, that increasing the gas-to-liquid momentum ratio, at a fixed liquid Reynolds number, yields a narrower spray, whose virtual origin is further upstream, and with an liquid core that is shorter, with smaller variations (in magnitude, the fluctuations as a percentage of the mean are constant) happening at faster time-scales. Adding swirl, i.e. diverting part of the longitudinal momentum into angular momentum for a fixed total gas Reynolds number, has a similar effect on the intact core, but an opposing effect on the spray structure in the near field, as long as the swirl ratio is within two threshold values for which a stable vortex can exist downstream of the intact core. The lower threshold, already identified in the literature, is between  $0.25 < SR_c^1 < 0.5$ , irrespective of  $M$  for the moderate to high momentum ratios considered here, in good agreement with [Hopfinger and Lasheras, 1996]. The upper threshold, newly identified in the current study for high swirl and low momentum ratios, is between  $0.75 < SR_c^2 < 1$  for  $M \leq 11$  and  $SR_c^2 > 1$  for  $M > 11$ .

The dramatic transition of the liquid core length PDF between  $M = 25$  and  $M = 80$  (Fig. 2a)), where both the average and standard deviation decrease strongly, along with the correlation time (Fig. 7), may be due to the transition, from an intact liquid core to a hollow core, referred to as a liquid crown [Machicoane et al., 2019], shedding ligaments from its periphery. The liquid core is a backwards-facing step for the gas, so that a vortex can form

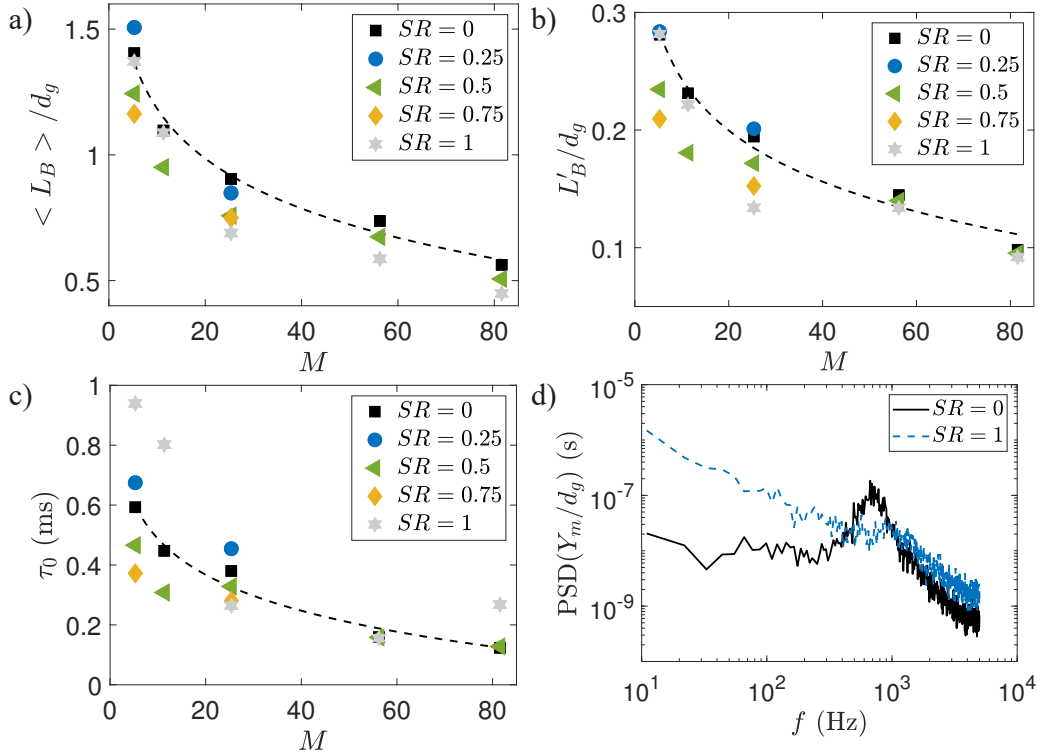


Figure 7: (color online) Evolution of the liquid core length mean  $\langle L_B \rangle$  (a), standard deviation  $L'_B$  (b) and timescale  $\tau_0$  (c) as a function of the momentum ratio  $M$ , for different swirl ratios  $SR$ . The dashed lines are fits along  $M$  for  $SR = 0$  of values  $\langle L_B \rangle = 1.85 \pm 0.22 - (0.29 \pm 0.07) \log(M)$ ,  $L'_B = 0.39 \pm 0.05 - (0.06 \pm 0.02) \log(M)$  and  $\tau_0 = 0.89 \pm 0.17 - (0.17 \pm 0.05) \log(M)$ . d) Raw PSD of the  $y$  coordinate of the center of area of the liquid core  $Y_m$  for  $M = 80$ ,  $SR = 0$  (with a peak around 700 Hz) and  $SR = 1$ .

partially inside of the liquid core, even in the absence of swirl, resulting in the crown shape. This can also explain why the evolution with swirl ratio is monotonic above the lower threshold for  $M = 25$ , a crown transition happening at  $SR = 0.5$  that would stabilize the vortex and prevent breakdown inside the nozzle, which does not happen at lower  $M$ . These changes in topology of the liquid core along the spray parameters may also account for the discrepancies between the proposed correlation of the liquid core length.

When  $SR \geq 0.5$  for  $M = 80^2$ , the liquid crown becomes unstable, exhibiting partial dewetting along the water nozzle circumference. For  $SR = 1$ , the crown is only attached to about two-third of the circumference, as the vortex penetrates inside of the liquid nozzle, pushing the liquid aside (see the video <http://depts.washington.edu/fluidlab/FEDSM2017video.shtml> at time stamp 1:48 s). The liquid-free portion of the water nozzle resembles then a backward facing step for the gas flow, and the vortex develops a long-time dynamics, as expected in this canonical flow where oscillations have been reported [Wee et al., 2004]. In the present case, the vortex slowly rotates around the nozzle axis, along the water needle perimeter. This can be observed when looking at the time evolution of the center of area of the liquid core, projected along the  $y$  axis,  $Y_m$  (see the inset of Fig. 8b) for an illustration of its detection). Figure 7d) shows the PSD of  $Y_m$  for  $M = 80$  in the absence of swirl for a stable liquid crown and for  $SR = 1$  where the crown

---

<sup>2</sup>The discrepancy between the values of  $M$  in this manuscript [5, 25, 80] and in [Machicoane et al., 2019] [6, 29, 90] are due to small changes in the values of  $U_g$  due to slight differences in the water nozzle diameters of the two sets of nozzles used for those investigations.

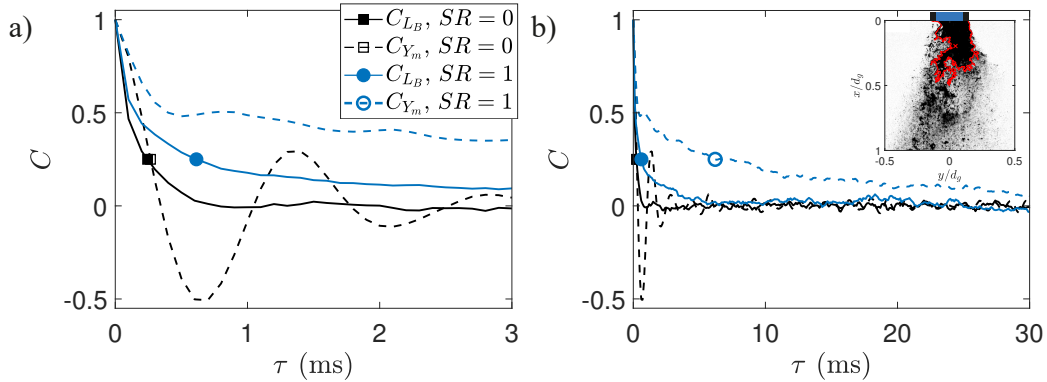


Figure 8: (color online) Auto-correlation function of both the liquid core length  $L_B$  (filled marker) and the  $y$  coordinate of the center of area of the liquid core  $Y_m$  (empty markers, dashed lines) over a narrow (a) and wider range (b) of the time-lag  $\tau$  for  $M = 80$ ,  $SR = 0$  and  $SR = 1$ . The symbols show the time at which the function reach a 0.25 threshold at 0.24, 0.27, 0.61 and 6.2 ms in the order of the legend.

is unstable. For  $SR = 0$ , the low-frequency range presents a plateau: no long-time dynamics is present and the signal is uncorrelated at long times. A peak is present at high frequencies, around 700 Hz, representing the fast transverse oscillations referred to as flapping. For  $SR = 1$ , while this high-frequency peak may still be present around 900 Hz, a power law of exponent of approximately  $-1.1$  is present at low frequencies over close to two decades, revealing the long-time dynamics of the vortex.

This long-time dynamics prevents decorrelation of  $Y_m$  (over time-scales that are relevant for the spray) and it affects the shape of the liquid core length auto-correlation function, as can be observed in Fig. 8. While decorrelation happens very quickly for  $SR = 0$ , it slows down in the presence of swirl and the shape of the function resembles the auto-correlation function  $C_{Y_m}$  for the  $y$  position of the liquid core center of area. This explains why

$\tau_0$  is much bigger for ( $M = 80, SR = 1$ ) than for ( $M = 80, SR = 0$ ) (while swirl addition decreases the correlation time for  $M < 80$ ). This phenomenon is also present for  $SR = 0.5$ , although its effect is less noticeable, as only partial dewetting is observed for this condition (and not a fully unstable liquid crown). In the absence of swirl,  $C_{Y_m}$  shows oscillations, in agreement with the high-frequency peak of the PSD, with a correlation time (extracted with the same method as for  $\tau_0$ ) of 0.18 ms, while it is 2.34 ms for  $SR = 1$ .

#### *4.2. Oscillating swirl*

Figure 9 shows the maps of the probability of liquid presence  $P$ , and of its variations  $P'$ , obtained through an ensemble average and standard deviation of the post-processed images, for three conditions at the same time-averaged momentum ratio of 25: no swirl, a steady swirl ratio of 0.5 and swirl oscillating between 0 and 1, with an average of  $\langle SR \rangle = 0.5$  (as described in Sec. 2.1). The corresponding values of the spray initial spreading angle  $\theta$  and virtual origin  $x_{VO}$  are reported in Table 2. Oscillations of the swirl seem to have little effect on the angle, which is less than 10% smaller than for a constant swirl, but still 35% bigger than the value in the absence of swirl, while the virtual origin is roughly in between these two cases. It can be expected to find similar values of  $\theta$  between  $SR = 0.5$  and  $\langle SR \rangle = 0.5$ , as the swirl ratio in the latter condition oscillates around the value of the former condition, yielding a spray that spreads alternatively wider and narrower around what is observed for the steady case. The contour of the liquid presence variations, set at an arbitrary threshold of  $P' = 0.4$  for clarity, underlines important temporal variations of the liquid presence over a large region, in the case of swirl oscillations. While swirl addition makes this

contour wider along  $y$  and shorter along  $x$  for the steady case  $SR = 0.5$  compared to  $SR = 0$ , it becomes much wider (but of the same longitudinal extent) when the swirl oscillates. One can also note that both regions with  $P = 1$  and with  $P' = 0$  are shortest in the latter case. Finally, as indicated by the black dots in the first row of Fig. 9, for  $\langle M = 25 \rangle$ , swirl addition extends the self-similar region of  $P$ , starting from  $x \geq 0.14d_g$  instead of  $0.17d_g$ , which is further enhanced when oscillations are present, with self-similarity starting from  $x \geq 0.09d_g$ . However, a constant swirl makes for a shorter linear spreading region within the near-field of the spray, as the angular momentum keeps centrifuging the spray droplets outwards radially as  $x$  increases.

As indicated by the observation of the maps of  $P$  and  $P'$ , the liquid core length is affected by swirl oscillations (Fig. 10). A snapshot of the time series over one oscillation period clearly shows a dynamics resembling a quasi-steady behavior,  $L_B$  fluctuating around an oscillating sliding average, as illustrated by the use of the moving mean. The response may seem quasi-steady at first glance but, when comparing the time series of Fig. 10a), it is apparent that there are significant deviations from this qualitative picture. First, one can observe that the liquid core length is shortest at approximately 0.2 seconds after the trough of the oscillation (indicated by the red arrow). Second, while smaller values of  $L_B$  at the peak of the oscillation are expected for  $M(t) = 45$  and  $SR(t) = 1$  than for  $(M = 25, SR = 1)$ , one can note that the maximum values observed are barely above those for  $(M = 25, SR = 1)$  and never above those for  $(M = 25, SR = 0)$ , while the troughs of the oscillation correspond to  $M(t) = 11$  and  $SR(t) = 0$ . This is confirmed when

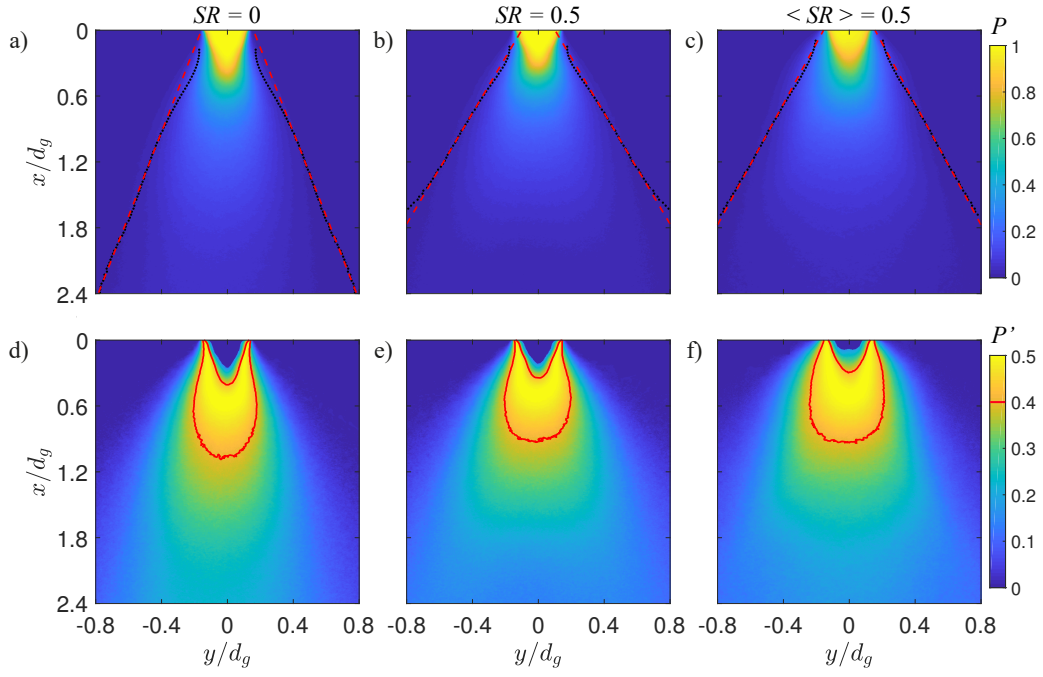


Figure 9: (color online) Probability (average of the thresholded image stack) of liquid presence (a-c) and its variations (standard deviation of the thresholded image stack) (d-f). The columns corresponds to  $M = 25$  and  $SR = 0$  (a, d),  $M = 25$  and  $SR = 0.5$  (b, e) and  $\langle M \rangle = 25$  and  $\langle SR \rangle = 0.5$  (c, f). a-c) The black dots and red dashed lines define the spray edge and initial angle (see Figure 5); d-f) The red line is a contour of the liquid presence variations being equal or higher than 0.4.

Case	$\theta$ ( $^\circ$ )	$x_{VO}/d_g$	$\langle L_B \rangle / d_g$	$L'_B/d_g$	$\tau_0$ (ms)
$SR = 0$	29.3	-0.6	0.9	0.19	.38
$SR = 0.5$	43.2	-0.26	0.76	0.17	.33
$\langle SR \rangle = 0.5$	39.9	-0.43	0.8	0.27	68.4

Table 2: Spray metrics for  $M = 25$ , in the absence of swirl  $SR = 0$ , for constant swirl  $SR = 0.5$  and for swirl oscillations  $\langle SR \rangle = 0.5$  (and  $\langle M \rangle = 25$ ). When a moving mean is subtracted along the time series in the latter case, the standard deviation of the redefined liquid core length and its timescale are  $l'_B = 0.19$  and  $\tau_0^{l_B} = 0.53$  ms.

comparing the PDFs of the whole time series in Fig. 10b) where, while the average value  $\langle L_B \rangle$  is found to be between both steady cases, the standard deviation  $L'_B$  is about 50% larger, corresponding to the presence of both much larger and much smaller lengths than the average (see Table 2).

The time dynamics on the liquid core length  $L_B(t)$  is largely driven, at large scales, by the swirl oscillations, which biases the shape of the auto-correlation function, as seen in Fig. 10c), where the correlation time  $\tau_0 = 68.4$  ms is more representative of the variations of the moving mean, than of the fluctuations around it. To study the latter, we define  $l_B(t) = L_B(t) - \overline{L_B(t)}^T$ , with  $T = 50$  ms, where  $\overline{L_B(t)}^T$  represents a moving mean computed over a sliding window of total length  $T$ . This enables the study of the magnitude and time-scale of these fluctuations, the former being of the same order than for both steady cases, and the latter being about 1.4 times larger than for ( $M = 25, SR = 1$ ).

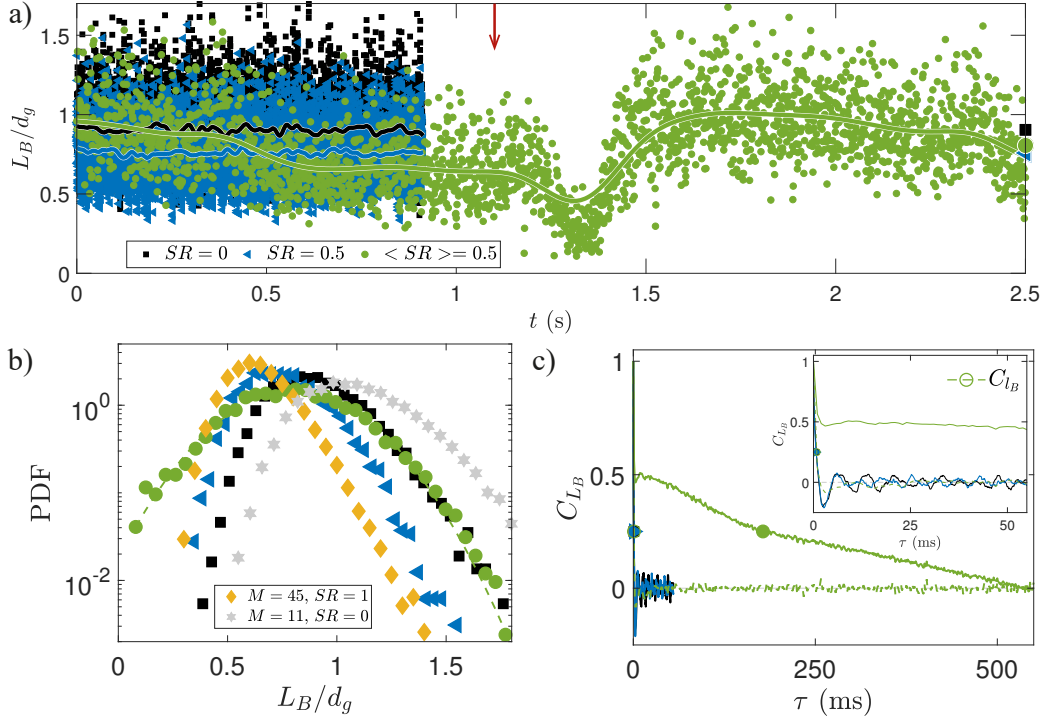


Figure 10: (color online) a) Time series of the liquid core length  $L_B$  normalized by the gas nozzle inner diameter  $d_g$  for  $M = 25$  and  $SR = 0$  (■),  $M = 25$  and  $SR = 0.5$  (◄) and  $\langle M \rangle = 25$  and  $\langle SR \rangle = 0.5$  (●). The thick lines show a moving mean and the corresponding symbols on the right vertical axis correspond to the time-averaged values over the whole series (only about a fourth of the time series is shown for the oscillating swirl condition that is recorded at a tenth of the frame rate but over 10 times the duration of the non-oscillating conditions). The red arrow indicates the time for the crest of one oscillation (local maximum of swirl and momentum ratio). b) Corresponding PDFs over the whole series, the dashed line is a Gaussian distribution defined by the mean and standard deviation of the liquid core length for the oscillating swirl condition. The PDFs for steady cases at the crest ( $M = 45$  and  $SR = 1$  ♦) and trough ( $M = 11$  and  $SR = 0$  ★) of the oscillation are added for comparison. c) Corresponding auto-correlation functions using the whole series. The additional green dashed lined represents the function calculated over the liquid core length subtracted by its moving average:  $l_B = L_B - \overline{L_B}(t)^T$  with  $T = 50$  ms, for the oscillating swirl case. In the latter case, the functions cross the 0.25 threshold at 178.1 ms for  $L_B$  and 0.85 ms for  $l_B$ .

## 5. Discussion

The statistical study of the liquid core length  $L_B$  in this paper allows for a discussion beyond just its temporal mean, to include both its moments and time dynamics. The PDFs of  $L_B$  already show that an increase of  $M$  strongly lowers the average and slightly diminishes the standard deviation, with a reduction of the probability of finding very large lengths (right-hand side tail of the PDFs), resulting in a slight decrease in skewness. Swirl addition presents the same general trend. While some periodicity is exhibited in the liquid core length time series for the low range of momentum ratios, at higher  $M$  the turbulence fluctuations make its measurement difficult and the study of the time-scale over which variations happen becomes more suitable through auto-correlation functions. Both increases in  $M$  and  $SR$  decrease the correlation time  $\tau_0$ . The study of the two first moments of the PDFs of the liquid core length, and its correlation time over the whole spray parameter range explored here, nuances the former statement. As demonstrated by [Hopfinger and Lasheras, 1996], a lower threshold of swirl ratio exists, below which no effect of swirl addition is observed on the spray. Some quantities,  $\tau_0$  in particular, actually show the opposite effect when very little swirl is added, as the little amount of angular momentum is not enough to form a coherent vortex behind the liquid core, and seems to inhibit the growth of instabilities slightly. Additional to this previously described lower threshold, an upper threshold is found for which the effects of swirl on the spray are either reduced (compared to what would be expected if a monotonic behavior was present) or negated. This threshold is in the range  $0.75 < SR < 1$  for  $M \leq 11$ , and for greater momentum ratios, we can only hypothesize that it may exist

beyond the explored range of swirl values (up to  $SR = 1$ ). We attribute the existence to the upper threshold to vortex breakdown happening inside the nozzle when the angular momentum in the gas can not be contained in a single stable vortex, as it is strained out of the nozzle.

At high gas-to-liquid momentum ratios, a change of topology happens for the liquid core, from an intact core shedding liquid inclusions from its perimeter and tip, to a hollowed-out crown, shedding inclusions exclusively from its periphery (forming the “crenellations” of the crown). A gas recirculation vortex is partially inside of the crown, and swirl addition can stabilize the vortex enough for it to enter the liquid nozzle and displace the liquid, so that it can only exit on a crescent-like section of the liquid needle. While the precise boundary of this transition in the  $(M, SR)$  space may depend on the exact nozzle geometry (the size of the lip formed between the liquid nozzle inner and outer radii), the vortex characteristics are expected to be universal, in analogy to what is observed in the canonical flow behind a backward-facing step [Armaly et al., 1983]. In the latter, the relevant metrics can indeed be normalized and collapsed using the step height and the inflow bulk velocity ( $U_g$  here). The vortex, however, does not remain stable at a given location, but it exhibits a long-time dynamics, slowly rotating along the liquid nozzle perimeter, making the crown unstable as well. While the swirl addition, from  $SR = 0$  to  $SR = 1$ , decreases the mean intact length by about 25%, the unstable nature of the crown does not produce the expected decrease of intact length standard deviation (that roughly remains constant) and correlation time. The latter actually increases significantly (by a factor of 2 compared to  $SR = 0$ ), as the long-time dynamics of the vortex affects not only the

crown position, but also  $\tau_0$ . A spectral analysis of the crown location of the center of area reveals no characteristic oscillation frequency, but rather a power law in the low-frequency range, as is typical in long-time dynamics emerging in turbulent systems (see [Benzi, 2005; Grandemange et al., 2013; López-Caballero and Burguete, 2013]). [Machicoane et al., 2019] found that the crown can remain in the same position for long times compared to the spray time-scales (longer than 300 ms, for  $M = 200$  and  $SR = 1$ , which was the limited acquisition time in that study). For ( $M = 80$ ,  $SR = 1$ ), residence times were found as long as 60 ms and as short as a few ms. While more statistics would be necessary to settle this question, the PDFs of the residence time of the liquid core are likely to be exponentially decreasing, as is common in such multi-stable systems [Berhanu et al., 2007; Machicoane et al., 2016; de la Torre and Burguete, 2007]. However, the auto-correlation function of  $Y_m$  reveals, with the available statistics, that the displacement of the liquid core varies with time-scales of the order of 2.3 ms, which is about 10 times longer than  $\tau_0$ . This indicates that, while the instability of the liquid core and its change of topology, from full crown to unstable partial crown, does affect the time-scale at which the liquid core length evolves, the long-time dynamics of the core position around the atomizer axis does not fully drive its length.

Slow-time oscillations of the swirl ratio were considered briefly, for a condition where the liquid core is expected to experience three states along the oscillations [Machicoane et al., 2019]: intact core, crown and unstable crown, from trough to crest. Despite the fact that the oscillation frequency is about 350 times slower than the slowest time-scales of the spray (i.e. the varia-

tion frequency of the liquid core length found in Fig.2b)), the behavior is not quasi-steady. The part of the liquid core length PDF that correspond to  $L_B \geq \langle L_B \rangle$  is, when swirl oscillates, almost overlapping the one in the absence of swirl for the same time-averaged momentum ratio  $\langle M \rangle = 25$ . However, these larger-than-average lengths are mostly present around the troughs of the oscillations, where  $M(t) = 11$  and  $SR(t) = 0$ , for which the associated steady condition presents much larger lengths. Additionally, while a constant swirl equal to the average value of the oscillating case does yield smaller probability of larger liquid core lengths (by a factor of about 5 for lengths equal to  $1.3d_g$ ), swirl oscillations can also produce much smaller lengths. For example, for a probability of 10%, swirl oscillations have lengths about 2.3 times smaller than those of steady swirl. The steady case of values of the crest ( $M = 45$ ,  $SR = 1$ ) has a much smaller mean and standard deviation, but the distribution is still slightly skewed toward larger lengths, while the PDF is Gaussian for swirl oscillations. For the same example of 10% probability, the corresponding lengths are actually about half the values for the steady case, and the smallest lengths measured, with a probability of 5%, are almost 4 times smaller for swirl oscillations. Of course, the probability of finding lengths of the order of  $0.6d_g$ , which corresponds to the most probable value for ( $M = 45$ ,  $SR = 1$ ), is about three time lower for the swirl oscillations case, but it does come at the cost of multiplying by 1.3 the time-averaged gas Reynolds number (corresponding to multiplying by 1.7 the momentum ratio). Despite the very large standard deviation observed for swirl oscillations, that are inherent to the very large variations of the swirl ratio, the spray seems to present a more stable behavior, with fluctuations around the moving mean

similar to steady cases, happening over slower time-scales. This may be due to the stabilization of the vortex downstream of the liquid core, induced by the slow flow pulsation.

## 6. Conclusions

Using high-speed shadowgraphy of the near-field of the spray produced by a canonical two-fluid coaxial atomizer, the structure of the spray and the dynamics of its intact liquid core were analyzed. A method was introduced to define an initial spreading angle in a robust manner without operator dependency. This spreading angle, while nominally dependent on the specific threshold chosen for the spray width, presents a behavior along relevant spray parameters that is independent of the threshold. A virtual origin, universally defined, completes a simple geometrical description of the spray structure in the near-field, that can be integrated into models. Increases of the gas-to-fluid momentum ratio, for a laminar liquid injection condition, decrease the spreading angle and push the virtual origin further upstream of the nozzle exit. The addition of swirl, above a lower threshold that stabilizes a vortex downstream of the liquid core by the helical gas jet, and below an upper threshold above which vortex breakdown happens inside of the gas nozzle, tends to increase the spreading angle, as reported in the literature. The virtual origin also increases with swirl, and can be found downstream of the atomizer exit plane at low  $M$ , or further downstream but still within the nozzle for  $M \geq 25$ .

The study of the liquid core length statistics through its probability density function and first two moments, and of the spray temporal dynamics

through auto-correlation functions leading to the definition of a correlation time, are presented for use in the creation of reduced-order model, in analogy with the stochastic models for single-phase turbulent flows [Sawford and Yeung, 2000]. The description of the evolution of the spray structure and the liquid core full statistics, over a wide range of gas-to-liquid momentum and swirl ratios, is a simple but efficient representation of the spray. Both increases of  $M$  and  $SR$  (within the lower and upper thresholds), lower the liquid core length average, standard deviation and correlation time. However, at high momentum ratio, swirl addition from  $SR = 0$  to  $SR = 1$  leads to a topology change of the liquid core, from full crown to unstable partial crown, that is off-centered from the atomizer axis by a vortex penetrating inside of the liquid nozzle, affecting the correlation time. The long-time dynamics, associated with the motion of the crown around the atomizer axis, is indeed affected with an increase in this correlation time.

The departure from a quasi-steady behavior of the spray for slow swirl temporal oscillations was briefly described. This is relevant for certain applications of coaxial atomization, when there is a cost of increasing the gas flow rate, but diverting it into a longitudinal and azimuthal component is possible. This could be especially true if lower amplitude oscillations of the swirl, which would be expected to lower the liquid core length standard deviation, prove as effective on the spray dynamics for such systems. Finally, characterizing the response of this turbulent multiphase flow to temporal perturbations, as done here, represents a key step to better understand the possibilities of feedback control implementations.

## 7. Acknowledgements

This work was sponsored by the Office of Naval Research (ONR) as part of the Multidisciplinary University Research Initiatives (MURI) Program, under grant number N00014-16-1-2617. The views and conclusions contained herein are those of the authors only and should not be interpreted as representing those of ONR, the U.S. Navy or the U.S. Government.

## References

- [Aliseda et al., 2008] Aliseda, A., Hopfinger, E. J., Lasheras, J. C., Kremer, D. M., Berchielli, A., and Connolly, E. K. (2008). Atomization of viscous and non-Newtonian liquids by a coaxial, high-speed gas jet. Experiments and droplet size modeling. *International Journal of Multiphase Flow*, 34(2), 161-175
- [Arai and Hashimoto, 1985] Arai, T., and Hashimoto, H. (1985). Behavior of gas-liquid interface on a liquid film jet: instability of a liquid film jet in a co-current gas stream. *Bulletin of JSME*, 28(245), 2652-2659.
- [Armaly et al., 1983] Armaly, B. F., Durst, F., Pereira, J. C. F., and Schönung, B. (1983). Experimental and theoretical investigation of backward-facing step flow. *Journal of fluid Mechanics*, 127, 473-496.
- [Benzi, 2005] Benzi, R. (2005). Flow reversal in a simple dynamical model of turbulence. *Physical review letters*, 95(2), 024502.
- [Billant et al., 1998] Billant, P., Chomaz, J. M., and Huerre, P. (1998). Ex-

- perimental study of vortex breakdown in swirling jets. *Journal of Fluid Mechanics*, 376, 183-219.
- [Berhanu et al., 2007] Berhanu, M., Monchaux, R., Fauve, S., Mordant, N., Pétrélis, F., Chiffaudel, A., Daviaud, F., Dubrulle, B., Marié, L., Ravetlet, F. and Bourgoïn, M. (2007). Magnetic field reversals in an experimental turbulent dynamo. *EPL (Europhysics Letters)*, 77(5), 59001.
- [Bracco, 1985] Bracco, F. V. (1985). Modeling of engine sprays. SAE Technical Paper (No. 850394).
- [Charalampous et al., 2007] Charalampous, G., Hardalupas, Y., and Taylor, A. (2007). A novel technique for measurements of the intact liquid jet core in a coaxial airblast atomizer. 45th AIAA Aerospace Sciences Meeting and Exhibit (p. 1337).
- [Charalampous et al., 2009] Charalampous, G., Hardalupas, Y., and Taylor, A. (2009). Structure of the continuous liquid jet core during coaxial air-blast atomisation. *International Journal of Spray and Combustion Dynamics*, 1(4), 389-415.
- [Charalampous et al., 2019] Charalampous, G., Hadjiyiannis, C., and Hardalupas, Y. (2019). Proper orthogonal decomposition of primary breakup and spray in co-axial airblast atomizers *Physics of Fluids*, 31(4), 043304.
- [Chigier, 1981] Chigier, N. A. (1981). *Energy, combustion, and environment*. New York: McGraw-Hill.

- [Chigier and Farago, 1992] Chigier, N., and Farago, Z. (1992). Morphological classification of disintegration of round liquid jets in a coaxial air stream. *Atomization and Sprays*, 2(2).
- [Chigier and Reitz, 1996] Chigier, N., and Reitz, R. D. (1996). Regimes of jet breakup and breakup mechanisms- Physical aspects. *Recent advances in spray combustion: Spray atomization and drop burning phenomena.*, 1, 109-135.
- [de la Torre and Burguete, 2007] de la Torre, A., and Burguete, J. (2007). Slow dynamics in a turbulent von Kármán swirling flow. *Physical review letters*, 99(5), 054101.
- [Delon et al., 2018] Delon, A., Cartellier, A., and Matas, J. P. (2018). Flapping instability of a liquid jet. *Physical Review Fluids*, 3(4), 043901.
- [Dumouchel, 2008] Dumouchel, C. (2008). On the experimental investigation on primary atomization of liquid streams. *Experiments in fluids*, 45(3), 371-422.
- [Engelbert et al., 1985] Engelbert, C., Hardalupas, Y., and Whitelaw, J. H. (1995). Breakup phenomena in coaxial airblast atomizers. *Proceedings of the Royal Society of London. Series A: Mathematical and Physical Sciences*, 451(1941), 189-229.
- [Eroglu et al., 1991] Eroglu, H., Chigier, N., and Farago, Z. (1991). Coaxial atomizer liquid intact lengths. *Physics of Fluids A: Fluid Dynamics*, 3(2), 303-308.

- [Gallaire and Chomaz, 2003] Gallaire, F., and Chomaz, J. M. (2003). Instability mechanisms in swirling flows. *Physics of fluids*, 15(9), 2622-2639.
- [Gorokhovski and Herrmann, 2008] Gorokhovski, M., and Herrmann, M. (2008). Modeling primary atomization. *Annu. Rev. Fluid Mech.*, 40, 343-366.
- [Grandemange et al., 2013] Grandemange, M., Gohlke, M., and Cadot, O. (2013). Turbulent wake past a three-dimensional blunt body. Part 1. Global modes and bi-stability. *Journal of Fluid Mechanics*, 722, 51-84.
- [Krolick and Owkes, 2018] Krolick, W., and Owkes, M. (2018). Primary atomization instability extraction using dynamic mode decomposition. *Atomization and Sprays*, 28(12).
- [Heindel, 2019] Heindel, T. J. (2019). X-ray Imaging Techniques to Quantify Spray Characteristics in the Near-Field. *Atomization and Sprays*, 29(1), 028797.
- [Hopfinger and Lasheras, 1996] Hopfinger, E. J., and Lasheras, J. C. (1996). Explosive breakup of a liquid jet by a swirling coaxial gas jet. *Physics of Fluids*, 8(7), 1696-1698.
- [Juniper and Candel, 2003] Juniper, M. P., and Candel, S. M. (2003). The stability of ducted compound flows and consequences for the geometry of coaxial injectors. *Journal of Fluid Mechanics*, 482, 257-269.
- [Kannan et al., 2018] Kannan, K., Kedelty, D., and Herrmann, M. (2018). An in-cell reconstruction finite volume method for flows of compressible immiscible fluids. *Journal of Computational Physics*, 373, 784-810.

- [Kastengren and Powell, 2014] Kastengren, A. L., and Powell, C. F. (2014). Synchrotron X-ray techniques for fluid dynamics. *Experiments in Fluids*, 55(3), 1686.
- [Kumar and Sahu, 2018] Kumar, A., and Sahu, S. (2018). Liquid jet breakup unsteadiness in a coaxial air-blast atomizer. *International Journal of Spray and Combustion Dynamics*, 10(3), 211-230.
- [Lasheras et al., 1998] Lasheras, J. C., Villermaux, E., and Hopfinger, E. J. (1998). Break-up and atomization of a round water jet by a high-speed annular air jet. *Journal of Fluid Mechanics*, 357, 351-379.
- [Lasheras and Hopfinger, 2000] Lasheras, J. C., and Hopfinger, E. J. (2000). Liquid jet instability and atomization in a coaxial gas stream. *Annual Review of Fluid Mechanics*, 32(1), 275-308.
- [Lefebvre, 1989] Lefebvre, A. H. (1989). *Atomization and Sprays*. Hemisphere Pub. Corp., New York.
- [Leroux, 2007] Leroux, B., Delabroy, O., and Lacas, F. (2007). Experimental study of coaxial atomizers scaling. Part I: dense core zone. *Atomization and Sprays*, 17(5).
- [Li et al., 2019] Li, D., Bothell, J. K., Morgan, T. B., Machicoane, N., Aliseda, A., Kastengren, A. L., and Heindel, T. J. (2019). Time-averaged spray analysis in the near-field region using broadband and narrowband X-ray measurements. *Atomization and Sprays*, 29(4), 331-349.

- [Liang and Maxworthy, 2005] Liang, H., and Maxworthy, T. (2005). An experimental investigation of swirling jets. *Journal of Fluid Mechanics*, 525, 115-159.
- [Lilley, 1977] Lilley, D. G. (1977). Swirl flows in combustion: a review. *AIAA journal*, 15(8), 1063-1078.
- [Ling et al., 2019] Ling, Y., Fuster, D., Tryggvason, G., and Zaleski, S. (2019). A two-phase mixing layer between parallel gas and liquid streams: multiphase turbulence statistics and influence of interfacial instability. *Journal of Fluid Mechanics*, 859, 268-307.
- [López-Caballero and Burguete, 2013] López-Caballero, M., and Burguete, J. (2013). Inverse cascades sustained by the transfer rate of angular momentum in a 3D turbulent flow. *Physical review letters*, 110(12), 124501.
- [Machicoane et al., 2016] Machicoane, N., López-Caballero, M., Fiabane, L., Pinton, J. F., Bourgoïn, M., Burguete, J., and Volk, R. (2016). Stochastic dynamics of particles trapped in turbulent flows. *Physical Review E*, 93(2), 023118.
- [Machicoane et al., 2019] Machicoane, N., Bothell, J. K., Li, D., Morgan, T. B., Heindel, T. J., Kastengren, A. L., and Aliseda, A. (2019). Synchrotron radiography characterization of the liquid core dynamics in a canonical two-fluid coaxial atomizer. *International Journal of Multiphase Flow*, 115, 1-8.

- [Marmottant and Villermaux, 2004] Marmottant, P., and Villermaux, E. (2004). On spray formation. *Journal of Fluid Mechanics*, 498, 73-111.
- [Odier et al., 2018] Odier, N., Balarac, G., and Corre, C. (2018). Numerical analysis of the flapping mechanism for a two-phase coaxial jet. *International Journal of Multiphase Flow*, 106, 164-178.
- [Osuna-Orozco et al., 2019] Osuna-Orozco, R., Machicoane, N., Huck, P. D., and Aliseda, A. (2019). Feedback control of coaxial atomization based on the spray liquid distribution. *Atomization and Sprays*, 29(6), 545-551.
- [Owkes et al., 2018] Owkes, M., Cauble, E., Senecal, J., and Currie, R. A. (2018). Importance of curvature evaluation scale for predictive simulations of dynamic gas-liquid interfaces. *Journal of Computational Physics*, 365, 37-55.
- [Rajamanickam and Basu, 2017] Rajamanickam, K., and Basu, S. (2017). Insights into the dynamics of spray-swirl interactions. *Journal of Fluid Mechanics*, 810, 82-126.
- [Santhosh et al., 2013] Santhosh, R., Miglani, A., and Basu, S. (2013). Transition and acoustic response of recirculation structures in an unconfined co-axial isothermal swirling flow. *Physics of Fluids*, 25(8), 083603.
- [Sawford and Yeung, 2000] Sawford, B. L., and Yeung, P. K. (2000). Eulerian acceleration statistics as a discriminator between Lagrangian stochastic models in uniform shear flow. *Physics of fluids*, 12(8), 2033-2045.

- [Varga et al., 2003] Varga, C. M., Lasheras, J. C., and Hopfinger, E. J. (2003). Initial breakup of a small-diameter liquid jet by a high-speed gas stream. *Journal of Fluid Mechanics*, 497, 405-434.
- [Vu et al., 2018] Vu L. X., Chiodi R., and Desjardins O., (2018). Effect of Momentum Flux Ratio on the Primary Breakup Dynamics of a Canonical Coaxial Atomizer with Comparison to X-ray Radiography. Institute for Liquid Atomization and Spray Systems. ICLASS 2018, 14th Triennial International Conference on Liquid Atomization and Spray Systems, Chicago, IL, USA, July 22-26, 2018.
- [Wang and Desjardins, 2018] Wang, S., and Desjardins, O. (2018). 3D numerical study of large-scale two-phase flows with contact lines and application to drop detachment from a horizontal fiber. *International Journal of Multiphase Flow*, 101, 35-46.
- [Wee et al., 2004] Wee, D., Yi, T., Annaswamy, A., and Ghoniem, A. F. (2004). Self-sustained oscillations and vortex shedding in backward-facing step flows: Simulation and linear instability analysis. *Physics of Fluids*, 16(9), 3361-3373.